Chapter 1
Finite Time Steady 2D Vector Field Topology

Anke Friederici, Christian Rössl, and Holger Theisel

Abstract
Vector Field Topology describes the asymptotic behavior of a flow in a vector field, i.e., the behavior for an integration time converging to infinity. For some applications, a segmentation of the flow in areas of similar behavior for a finite integration time is desired. We introduce an approach for a finite-time segmentation of a steady 2D vector field which avoids the systematic evaluation of the flow map in the whole flow domain. Instead, we consider the separatrices of the topological skeleton and provide them with additional information on how the separation evolves at each point with ongoing integration time. We analyze this behavior and its distribution along a separatrix, and we provide a visual encoding for it. The result is an augmented topological skeleton. We demonstrate the approach on several artificial and simulated vector fields.

1.1 Introduction

Vector Field Topology has been established as one of the standard approaches to visualizing steady vector fields. Its main idea is simple and appealing: separate the field into regions of similar asymptotic flow behavior. This way, even complex flow structures can be represented by a low number of graphical primitives. In addition to this separation, Vector Field Topology has an attractive property in terms of computation: to get the whole segmentation, it is not necessary to consider every point in the domain. Instead, only a few points in the domain have to be touched (critical points, boundary switch points), and a few special stream lines starting from these points (separatrices) have to be computed.

Several approaches have been proposed to extend Vector Field Topology to unsteady fields. The main problem for this is that an asymptotic behavior cannot be

Anke Friederici
University of Magdeburg, e-mail: anke.friederici@st.ovgu.de

analyzed any more: unsteady fields usually allow an integration over a finite time only. Lagrangian Coherent Structures (LCS) provide such a segmentation of the field after a finite integration time. The perhaps most prominent example for LCS are ridge structures in Finite Time Lyapunov Exponents (FTLE) fields. In general, LCS computation requires a dense computation of the flow map in the whole domain.

In recent years there are approaches to compute LCS of unsteady fields by using steady Vector Field Topology [1, 42]. The main idea is to subtract a certain background flow field (or consider a certain reference frame) and reduce this way the computation of LCS of an unsteady field to the computation of steady Vector Field Topology. While these approaches are appealing, they have a fundamental problem: a segmentation for a finite integration time is computed by considering the asymptotic behavior of another flow, i.e., by considering an integration time converging to infinity. In general, integrating a (modified) field until infinity should not be considered for unsteady fields because it works with information that is not present in the data.

This paper solves the problem mentioned above: we present an approach to a finite time flow segmentation in a steady 2D field where we do not have to evaluate the flow map in the whole domain. (By applying a flow map evaluation everywhere, the potential advantage of the approaches in [1, 42] is lost; in this case one could do an LCS analysis of the original field directly without subtracting a certain flow.) We start with the assumption that the relevant separation takes place along the separatrices even for a finite integration time. For them, we compute the separation perpendicular to the flow either in a local or in a discretized global way. The results are characteristic functions (here called *separation functions*) which provide information about the separation along a separatrix. After evaluating these functions for a finite time and setting them in relation to their behavior when integrating towards infinity, we provide a simple visual encoding for them. In summary, we keep the benefits of steady vector field topology, which is stable and well-defined, while adding a scalar separation quantity.

1.2 Related Work

Topological methods for 2D vector fields have been introduced to the visualization community in [10]. Later they were extended to higher order critical points [28], boundary switch points [2], and closed separatrices [43]. In addition, topological methods have been applied to simplify [2, 3, 34, 35], smooth [41], compress [18, 17, 32] and construct [31, 38] vector fields. 3D topological feature are considered in [6, 11, 19, 20, 33, 37]. State-of-the-Art-Reports on topological methods for flow visualization can be found in [13, 14, 21].

Topological methods can be applied only to steady vector fields because they require an integration until infinity. For unsteady fields, Lagrangian Coherent Structures (LCS) have been established to find regions of homogeneous flow behavior. One of the most prominent approaches for this is the computation of ridge structures in FTLE fields, as introduced by Haller [7, 9]. To consider spatial separation only, Pobitzer et al. [22] weighted FTLE values by their angle to the separation direction. FTLE ridges were proposed for a variety of applications [8, 15, 30, 40]. Shadden et al. [29] showed that ridges of FTLE are approximate material structures, i.e., they converge to material structures for increasing integration times. This fact was used in [27, 36] to extract topological structures and in [16] to accelerate the FTLE computation in 2D flows. Also in the visualization community, different approaches have been proposed to increase performance, accuracy and usefulness of FTLE as a visualization tool [4, 5, 23, 25, 26].

In recent years approaches have evolved that aim at finding suitable moving frames of the underlying coordinate system to study the flow [1, 42]. This way, finite-time studies of time-dependent fields is lead back to a topological analysis of a derived steady field. This paper targets towards these approaches: by being able to analyze the finite-time behavior of steady fields without a dense sampling of the flow map, we make steady topology an appropriate tool also for a finite-time analysis.

1.3 The Approach

We start with an argumentation why we restrict the search for separating structures in steady flows to separatrices, i.e., the separating structures for integration times converging to infinity.

While it is not formally proven yet that separatrices and separation structures of LCS methods coincide [24], they behave similarly in general. The FTLE field and topological skeleton of our most complex dataset is shown in Figure 1.9. As can be seen, the FTLE ridges and separatrices overlap.

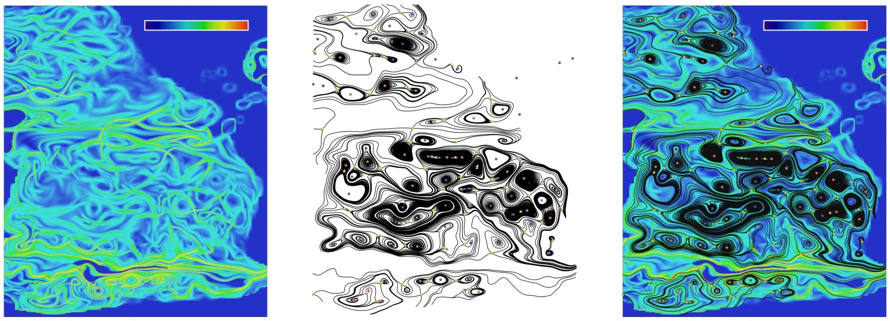

(a) FTLE (b) Topological skeleton (c) Combined image

Fig. 1.1: FTLE field and topological skeleton of the ocean dataset. a) Maximum of forward and backward integrated FTLE. b) Topological skeleton integrated starting from the saddles. c) Topological skeleton superimposed on FTLE image. The separatrices coincide with the FTLE ridges.

Notation

In the following, we consider a 2D steady vector field $\mathbf{v}$. Let $\mathbf{J}$ be its Jacobian. We assume that $\mathbf{J}$ is bounded, i.e., $\|\mathbf{J}\|$ does not exceed a certain fixed maximal value in the whole domain. Furthermore, let $\phi(\mathbf{x},\tau) : \mathbb{R}^2 \times \mathbb{R} \to \mathbb{R}^2$ denote the flow map of $\mathbf{v}$. Then a stream line is a parametric curve $\phi(\mathbf{x},\tau)$ starting from $\mathbf{x}$. The gradient of the flow map is denoted $\nabla\phi$. Furthermore we use the normalized perpendicular vector field

$$\mathbf{w}(\mathbf{x}) = \frac{1}{||\mathbf{v}||} \begin{pmatrix} 0 & -1 \\ 1 & 0 \end{pmatrix} \cdot \mathbf{v}(\mathbf{x}) \ . \tag{1.1}$$

Note that $\mathbf{w}$ has unit length and is defined for non-critical points only. This is not a serious restriction because stream lines starting in critical points do not leave them and are not considered.

1.3.1 The separation function for stream lines

Given a stream line, we analyze the separation along it. For this we focus on a separation perpendicular to the flow while removing the separation along the flow. To consider the separation along the stream line $\phi(\mathbf{x},\tau)$, we integrate a second stream line $\phi(\mathbf{x}_1,\tau)$ with the starting point

$$\mathbf{x}_1 = \mathbf{x} + \varepsilon_1 \, \mathbf{w}(\mathbf{x})$$

Then we consider $\varepsilon(\tau)$ as the distance of $\phi(\mathbf{x}_1,\tau)$ to the straight line $\phi(\mathbf{x},\tau) + \lambda \, \mathbf{v}(\phi(\mathbf{x},\tau))$ for $\lambda \in \mathbb{R}$:

$$\varepsilon(\tau) = \mathbf{w}(\phi(\mathbf{x},\tau))^T \, (\phi(\mathbf{x}_1,\tau) - \phi(\mathbf{x},\tau)).$$

Figure 1.2 illustrates this. We define the *separation function* of the stream line $\phi(\mathbf{x},\tau)$

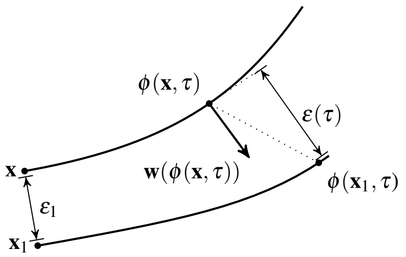

Fig. 1.2: Configuration for defining $s(\mathbf{x},\tau)$

as

$$s(\mathbf{x},\tau) = \lim_{\varepsilon_1 \to 0} \ln \frac{\varepsilon(\tau)}{\varepsilon_1} \ . \tag{1.2}$$

Keeping in mind that

$$\lim_{\varepsilon_1 \to 0} \frac{\phi(\mathbf{x}_1,\tau) - \phi(\mathbf{x},\tau)}{\varepsilon_1} = \nabla\phi(\mathbf{x},\tau) \cdot \mathbf{w}(\mathbf{x}) \ ,$$

(1.2) can be written as

$$s(\mathbf{x},\tau) = \ln\left(\mathbf{w}(\phi(\mathbf{x},\tau))^T \nabla\phi(\mathbf{x},\tau) \cdot \mathbf{w}(\mathbf{x})\right) \ . \tag{1.3}$$

Eq. (1.2) already gives a way to numerically compute the separation function: choosing a sufficiently small ε_1 for estimating the directional derivative of ϕ, the term $\ln \frac{\varepsilon(\tau)}{\varepsilon_1}$ is an approximation of s. However, its computation depends strongly on the choice of ε_1. If ε_1 is too small, (1.2) may run into numerical problems. If ε_1 is too large, $\mathbf{x}_1$ tends to move out of the linear neighborhood of $\mathbf{x}$. Fortunately, there is a localized version of s which avoids a discretization of the directional derivative of the flow map:

$$s(\mathbf{x},\tau) = \int_0^\tau \mathbf{w}(\phi)^T \mathbf{J}(\phi)\, \mathbf{w}(\phi)\, dr \tag{1.4}$$

with $\phi = \phi(\mathbf{x},r)$. In order to prove that (1.3) and (1.4) are identical, we have to show that

$$\frac{\partial}{\partial\tau}\left(\ln\left(\mathbf{w}(\phi)^T \nabla\phi\, \mathbf{w}(\mathbf{x})\right)\right) = (\mathbf{w}(\phi))^T \cdot \mathbf{J}(\phi)\mathbf{w}(\phi)$$

with $\phi = \phi(\mathbf{x},\tau)$. This can be shown by a straightforward application of elementary differentiation rules.

Note that (1.4) has some similarities to the local FTLE computation in [12]. In fact, [12] integrates the gradient of the flow map by a repeated matrix multiplication, leading to the fact that integrated measures can exponentially grow/shrink with increasing integration time. Contrary, (1.4) is a repeated addition of scalar values for the numerical integration.

Also note that s does not necessarily capture the maximal distortion in the neighborhood of a particle. Instead, it describes the distortion into one particular direction: perpendicular to the flow direction. For the evaluation of s on separatrices only, this derivative would generally give a close to maximal distortion.

Properties of the separation function: We list some properties of s. They can be shown by considering either (1.2), (1.3), (1.4).

- $s(\mathbf{x},0) = 0$ (follows from (1.2) and $\varepsilon(0) = \varepsilon_1$).
- $s(\mathbf{x},\tau)$ grows at most linearly with increasing τ. (To show this, we have to show that $\frac{ds}{d\tau}$ is bounded. This follows directly from (1.4) and the boundedness of $\mathbf{J}$.)
- s is additive: $s(\mathbf{x},\tau_1+\tau_2) = s(\mathbf{x},\tau_1) + s(\phi(\mathbf{x},\tau_1),\tau_2)$ (follows from (1.4)).

- For two points $\mathbf{x}$, $\mathbf{y}$ on the same stream line, their separation functions differ only by a translation: let $\mathbf{y} = \phi(\mathbf{x}, \tau_{\mathbf{y}})$. Then $s(\mathbf{y}, \tau) = s(\mathbf{x}, \tau + \tau_{\mathbf{y}}) - s(\mathbf{x}, \tau_{\mathbf{y}})$ (follows from the point above).
- s is inverted under backward integration: $s(\mathbf{x}, \tau) = -s(\phi(\mathbf{x}, \tau), -\tau)$ (follows from (1.4)).

1.3.2 The separation function for separatrices

Up to now, the separation function was defined for an arbitrary streamline. In this section, we show that the separation function has a special behavior for separatrices induced by a saddle point. Let $\mathbf{x}$ be on a separatrix, i.e., $\phi(\mathbf{x}, \tau)$ converges under forward integration to a saddle point $\mathbf{c}$ for $\tau \to \infty$. Then $s(\mathbf{x}, \tau)$ converges to a linear function for $\tau \to \infty$:

$$\lim_{\tau \to \infty} s(\mathbf{x}, \tau) = a\, \tau + b(\mathbf{x}) \tag{1.5}$$

where the slope a is determined by the Jacobian $\mathbf{J_c}$ of $\mathbf{v}$ in the saddle point $\mathbf{c}$. Let $\lambda_1 < 0 < \lambda_2$ be the eigenvalues of $\mathbf{J_c}$ and $\mathbf{e}_1, \mathbf{e}_2$ be the corresponding normalized eigenvectors. Then

$$a = (\mathbf{e}_1^{\perp})^T\, \mathbf{J_c}\, \mathbf{e}_1^{\perp} \tag{1.6}$$

where $\mathbf{e}_1^{\perp}$ is the vector $\mathbf{e}_1$ rotated by $\frac{\pi}{2}$ that is perpendicular to $\mathbf{e}_1$.

Figure 1.3 gives an illustration. The proofs of (1.5) and (1.6) are obtained by in the following way: since we are interested in the asymptotic behavior around a saddle, we can consider a linear vector field having a saddle with the desired Jacobian at the desired locations. Then the flow map and its derivatives can be written in a closed form, allowing to show (1.5) and (1.6) by simple computations.

The parameter $b(\mathbf{x})$ can be considered as a measure on how far s is away from its final linear behavior as $\tau \to \infty$. We will use this parameter for characterizing the separation. Note that for a particular point $\mathbf{x}$ on the separatrix, the computation of $b(\mathbf{x})$ is cumbersome because it requires an accurate integration towards the saddle. In order to get a more stable computation of $b(\mathbf{x})$, we formulate:

Theorem 1. *Given are two points* $\mathbf{x}$, $\mathbf{y}$ *on the same separatrix such that* $\mathbf{y} = \phi(\mathbf{x}, \tau_{\mathbf{y}})$. *Then*

$$b(\mathbf{y}) = b(\mathbf{x}) + s(\mathbf{x}, \tau_{\mathbf{y}}) - a\, \tau_{\mathbf{y}}.$$

The sketch of the proof is in Figure 1.4. Theorem 1 provides a way to compute b along a whole separatrix: given a saddle point $\mathbf{c}$, we start the integration of the separatrix at a point $\mathbf{x}_0 = \mathbf{c} + \varepsilon_0\, \mathbf{e}_1$. Note that ε_0 has to be chosen small enough such that $\mathbf{x}_0$ can be assumed to be in the linear neighborhood of $\mathbf{c}$. This assumption gives $b(\mathbf{x}_0) = 0$. From this we compute the separatrix by backward integration, i.e., we consider $\phi(\mathbf{x}_0, \tau)$ for $\tau \in\,]-\infty, 0]$. This way we get

$$b(\phi(\mathbf{x}_0, \tau)) = \begin{cases} 0 & \text{for } \tau \geq 0 \\ s(\mathbf{x}_0, \tau) - a\, \tau & \text{for } \tau < 0 \end{cases}$$

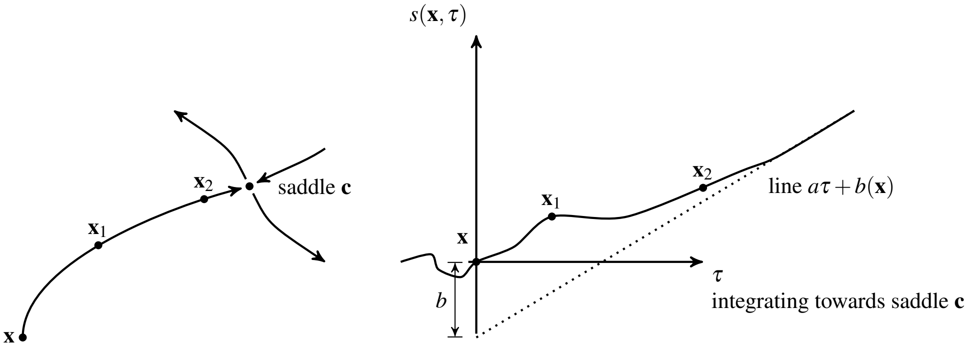

Fig. 1.3: Behavior of $s(\mathbf{x},\tau)$ for a separatrix.

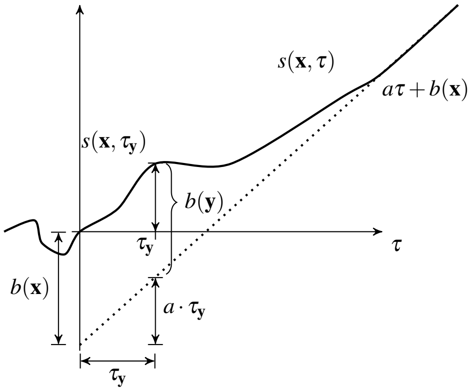

Fig. 1.4: Sketch for proof of theorem 1

where a is computed as (1.6). Note that $b(\mathbf{x})$ does not depend on the location of $\mathbf{x}$ as long as $\mathbf{x}_0$ is in the linear neighborhood of the saddle.

1.3.3 Properties and visualization of b

The number $b(\mathbf{x})$ for a point $\mathbf{x}$ on a separatrix is a measure of how the separation behaves when $\mathbf{x}$ is integrated towards the saddle. It gives a measure of how far the separation is away from the final asymptotic separation after integrating only a finite time. In a linear neighborhood of the saddle we have $b(\mathbf{x}) = 0$: starting an integration there leads to an exponential separation that is determined by the eigenvalues of the Jacobian of the saddle. For $\mathbf{x}$ in a certain distance of the saddle, $b(\mathbf{x})$ is a measure on how far $\mathbf{x}$ is from the final exponential separation for shorter integration time.

Note that $b(\mathbf{x})$ is *not* a local measure: instead it contains the essence of the separation behavior for a finite integration time when starting at $\mathbf{x}$.

In order to visualize b, we use the visual metaphor of a wall: instead of a 2D separating line, we render an extruded 3D surface where its height is connected to the strength of separation. For this, we introduce as height of the wall:

$$h(\mathbf{x}) = a\, e^{k\, b(\mathbf{x})}$$

where $k > 0$ is a degree of freedom for the visualization. This way we have $h(\mathbf{x}) = a$ in a linear neighborhood of a saddle, denoting the strength of the local separation at the saddle. The parameter k indicates how strong the height diminishment of the wall is when $b(\mathbf{x})$ deviates from 0. A small k gives that the height of the wall reflects strong deviation of b, a larger k brings the focus on small deviations of b from 0. We show examples of different choices of k in section 1.4.

1.3.4 Details and implementation

We determine critical points and classify saddles in a preprocess using a standard method [39]. They determine the starting points of separatrices. The computation of $s(\mathbf{x}, \tau)$ requires the numerical solution of an initial value problem. We apply a standard Runge-Kutta method in two passes. The first step is a standard streamline integration that yields a discrete curve representation of $\phi(\mathbf{x}, \tau)$ for starting at a point $\mathbf{x}_0$ near a saddle in the initial direction given by some eigenvector of the Jacobian at the critical point. We use a fourth-order Runge-Kutta method with step size adaptation that provides the streamline ϕ as a cubic C^1-continuous spline. The second step integrates the projection of the directional derivative, i.e., we apply the same Runge-Kutta method for the numerical integration of a scalar field. Finally, $b(\mathbf{y})$, and thus the height function $h(\mathbf{y})$, is computed by evaluating the separation function $s(\mathbf{x}_0, \tau)$ for $\mathbf{x}_0$ and $\tau_{\mathbf{y}}$. Note that the evaluation is backwards in time (see discussion of Theorem 1), i.e., there is no need for a reparametrization of ϕ or s as both were in fact computed by backward integration.

For visualization, we use standard line integral convolution to provide a global overview of the vector field $\mathbf{v}$ an underlying image. The separatrices are planar curves in the image. We lift each separatrix by interpreting the values $h(\mathbf{x})$ as height; this gives a second curve. We render all curves as tubes and connect the separatrix and its lifted counterpart by semitransparent surfaces. The critical points are the start and end points of curves and are emphasized by cylindrical structures with height h. Figure 1.6 shows an example.

1.4 Results

We compute and visualize the separation function for a number of vector fields.

Simple example. The first vector field is a piecewise linear function on a small 12×3 grid. The construction of the dataset is shown in Figure 1.5. For each vertex of the grid, we prescribe a vector such that bilinear interpolation in cells forms source (left) and saddle (right), and the center region yields a converging flow. The next

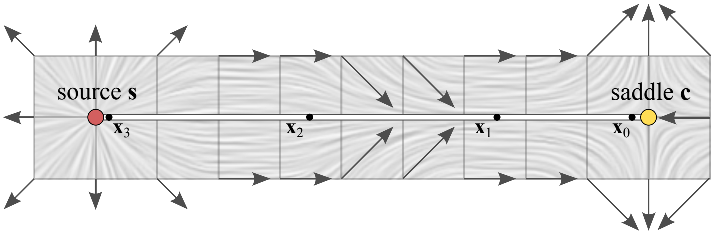

Fig. 1.5: Construction of a simple vector field on a 12×3 grid with a source and a saddle and a region of converging flow between. The velocity at the vertices are interpolated bilinearly within grid cells.

Figure 1.6 visualizes the separation function as described in the previous section. The white tubes show the separatrix in the plane and lifted by the height function h, and all pairs of curve are connected by semitransparent walls. Figure 1.7a shows the graph

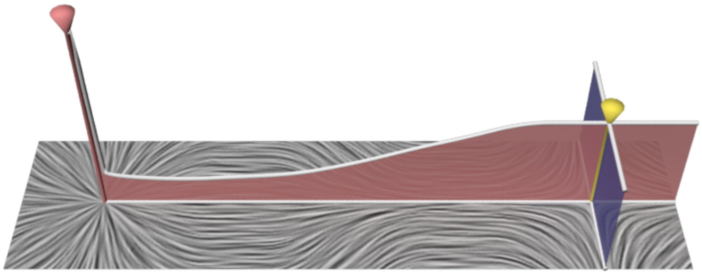

Fig. 1.6: Visualization of separation function as "height" h. The planar and lifted separatrices are connected by semitransparent walls.

of the separation function $s(\mathbf{x}, \tau)$ for the separatrix from the source to the saddle. It shows, from left to right, that the flow is diverging from the source in the beginning. Then there is region without separation followed by a region with converging flow. As the separatrix approaches the saddle, s shows asymptotic behavior of a line. The graph of h is parametrized over integration time. To visualize the distortion of the space-time map $\tau_{\mathbf{x}}$, Figure 1.5 shows positions of equally spaced samples $\mathbf{x}_0, \ldots, \mathbf{x}_3$ of the separatrix, and Figure 1.7a shows the associated times τ_{vx_i}.

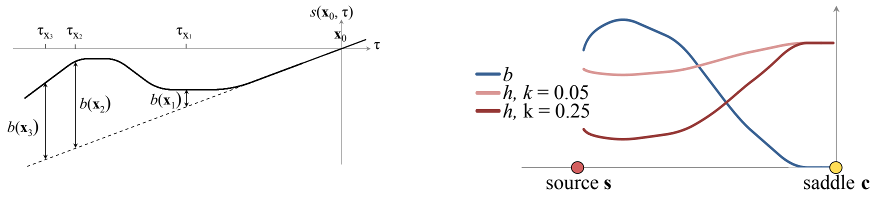

(a) Graph of $s(\mathbf{x}, \tau)$

(b) Graphs of b and h for varying k

Fig. 1.7: Behavior of s and h. a) Graph of separation function s along the separatrix. b) Graphs of two height function h for different values of k. Both heights h are a exponential function of b, which is also shown.

Figure 1.7b compares the graphs of the height function h for different values of the user parameter k.

Random Grid. Figure 1.8b shows results for a vector field generated from bilinear interpolation of vectors that were randomly chosen at the vertices of a 5 × 5 grid.

Slice of Rayleigh-Bénard convection cells. Figure 1.8a visualizes separation for a vertical slice through a Rayleigh-Bénard convection. The selected region of interest shows 16 critical points. The vector field is given as samples on a regular 64 × 64 grid, which are interpolated bilinearly.

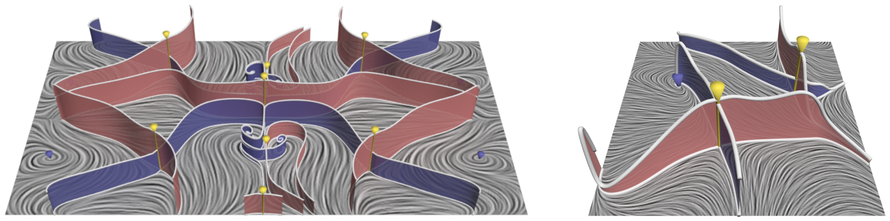

(a) Rayleigh-Bénard convection cell dataset

(b) Random vector field

Fig. 1.8: Visualization of two datasets. a) Vertical slice through a Rayleigh-Bénard convection cell dataset with 16 critical points. b) Separation walls for a random vector field interpolated on a 5 × 5 grid.

Slice of an ocean simulation. Figure 1.9 shows one slice from a simulation of the south pacific ocean. 150 critical points are present, from which 277 separatrices have been integrated. This number of walls being shown allows for an overall image of the dataset as well as the analysis of single separating structures. In the front of

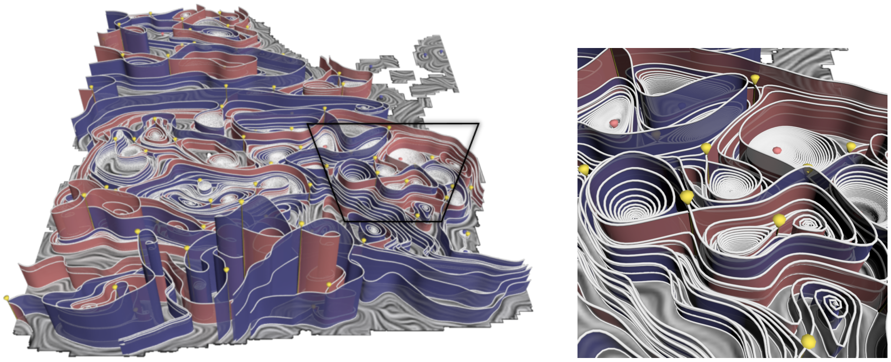

(a) Visualization of the full dataset.

(b) Close-up on swirling structures.

Fig. 1.9: Simulated ocean dataset with 150 critical points.

Figure 1.9a the walls are significantly higher than in the back, while the separation in the regions further away is so small that no wall is visible. This way, the highlight is set to the relevant structures with high separation.

Figure 1.9b shows a close-up on the walls of some swirling regions. Their behavior when moving near the critical point varies: some stay on a constant level, while others show diminishing separation.

1.5 Discussion and Limitations

The separation function s depends on the choice of ε_0, which tells how far $\mathbf{x}_0 = \mathbf{c} + \varepsilon_0 \mathbf{e}_1$ is located from the saddle, which in turn determines, how far the separatrix is integrated forward in time starting from the source. For $\varepsilon_0 \to 0$ we have $\tau_{\mathbf{x}_0} \to \infty$. At the same time we constructed s such that it converges to a linear function as $\phi(\mathbf{x}, \tau)$ approaches $\mathbf{c}$. The slope of this line decreases for decreasing ε_0. However, the exact slope is not of particular interest: All we require is arriving in the region of asymptotic behavior of s, which is typically achieved for small ε_0. This is because we are mainly interested in the behavior of $b(\mathbf{x})$, which is *invariant* to the slope of s (and hence ε_0) and *outside* the region of asymptotically linear s.

We don't visualize $b(\mathbf{x})$ directly but use an exponential scaling to obtain the height function $h(\mathbf{x})$. This scaling introduces additional parameters a and k. The first parameter a is a global scale, and k steers the exponential fall-off, which puts emphasis on different ranges of b.

The examples in the previous section range from simple constructed vector field to one with moderately complex topology. While the proposed method would work also for more and fairly complex vector fields, the visualization will not "scale" well. There are two reasons for this. First, the rendering of walls as semitransparent surface leads to problems with occlusion. This could partially be alleviated by advanced rendering techniques, e.g., steering transparency, or simply by displaying height walls only for selected separatrices. The second reason is more fundamental: Generally, all topology-based visualization methods are known to work well as long as the topological structure of the data is not too complex. This is the case, e.g., for noisy or turbulent vector fields. They typically show a vast number of critical points and a complex network of separatrices that is not suited for direct visualization. Our method shares this limitation with other topology-based visualization methods.

1.5.1 Future research

As future research, the approach can be extended to 2D steady divergence-free fields where a separatrix from a saddle re-enters the saddle again. Also, the finite-time separation of other separating structures such as closed stream lines and boundary switch curves should be analyzed. The extension to 3D is a challenging problem. Here, the finite time behavior of separating surfaces has to be studied. By replacing $\mathbf{w}$ in (1.1) by the normalized surface normal field of the separating surface, all following computations hold for 3D as well. The actual challenge is the visual representation of $h(\mathbf{x})$ since a wall-metaphor is not appropriate in 3D.

Acknowledgments

We thank Niklas Röber and Michael Böttinger from the DKRZ for providing the South Pacific ocean dataset.

References

1. H. Bhatia, V. Pascucci, R.M. Kirby, and P.-T. Bremer. Extracting features from time-dependent vector fields using internal reference frames. In *Computer Graphics Forum (Proceedings of EuroVis)*, volume 33, pages 21–30, June 2014.
2. W. de Leeuw and R. van Liere. Collapsing flow topology using area metrics. In *Proc. IEEE Visualization '99*, pages 149–354, 1999.
3. W. de Leeuw and R. van Liere. Visualization of global flow structures using multiple levels of topology. In *Data Visualization 1999. Proc. VisSym 99*, pages 45–52, 1999.
4. C. Garth, G. Li, X. Tricoche, C.D. Hansen, and H. Hagen. Visualization of coherent structures in transient 2d flows. In *Proceedings of TopoInVis*, 2007.
5. Christoph Garth, Florian Gerhardt, Xavier Tricoche, and Hans Hagen. Efficient computation and visualization of coherent structures in fluid flow applications. *IEEE Transactions on Visualization and Computer Graphics*, 13(6), 2007.
6. A. Globus, C. Levit, and T. Lasinski. A tool for visualizing the topology of three-dimensional vector fields. In *Proc. IEEE Visualization '91*, pages 33–40, 1991.
7. G. Haller. Distinguished material surfaces and coherent structures in three-dimensional fluid flows. *Physica D*, 149:248–277, 2001.

8. G. Haller. Lagrangian coherent structures from approximate velocity data. *Physics of Fluids*, 14(6), 2002.
9. G. Haller and G. Yuan. Lagrangian coherent structures and mixing in two-dimensional turbulence. *Physica D*, 147(3-4), 2000.
10. J. Helman and L. Hesselink. Representation and display of vector field topology in fluid flow data sets. *IEEE Computer*, 22(8):27–36, August 1989.
11. J. Helman and L. Hesselink. Visualizing vector field topology in fluid flows. *IEEE Computer Graphics and Applications*, 11:36–46, May 1991.
12. Jens Kasten, Christoph Petz, Ingrid Hotz, Bernd R. Noack, and Hans-Christian Hege. Localized finite-time lyapunov exponent for unsteady flow analysis. In Marcus Magnor, Bodo Rosenhahn, and Holger Theisel, editors, *Vision Modeling and Visualization*, volume 1, pages 265 – 274, 2009.
13. Robert S. Laramee, Helwig Hauser, L. Zhao, and Frits H. Post. Topology-based flow visualization, the art. In Helwig Hauser, Hans Hagen, and Holger Theisel, editors, *Topology-Based Methods in Visualization*. Springer Verlag, Mathematics and Visualization Series, 2007. (note 978-3-540-70822-3).
14. RobertS. Laramee, Helwig Hauser, Lingxiao Zhao, and FritsH. Post. Topology-based flow visualization, the state of the art. In Helwig Hauser, Hans Hagen, and Holger Theisel, editors, *Topology-based Methods in Visualization*, Mathematics and Visualization, pages 1–19. Springer Berlin Heidelberg, 2007.
15. Francois Lekien, Chad Coulliette, Arthur J. Mariano, Edward H. Ryan, Lynn K. Shay, George Haller, and Jerry Marsden. Pollution release tied to invariant manifolds: A case study for the coast of florida. *Physica D*, 210(1), 2005.
16. Doug Lipinski and Kamran Mohseni. A ridge tracking algorithm and error estimate for efficient computation of lagrangian coherent structures. *Chaos: An Interdisciplinary Journal of Nonlinear Science*, 20(1), 2010.
17. S. Lodha, N. Faaland, and J. Renteria. Topology preserving top-down compression of 2d vector fields using bintree and triangular quadtrees. *IEEE Transactions on Visualization and Computer Graphics*, 9(4):433–442, 2003.
18. S.K. Lodha, J.C. Renteria, and K.M. Roskin. Topology preserving compression of 2D vector fields. In *Proc. IEEE Visualization 2000*, pages 343–350, 2000.
19. K. Mahrous, J. Bennett, B. Hamann, and K. Joy. Improving topological segmentation of three-dimensional vector fields. In *Data Visualization 2003. Proc. VisSym 03*, pages 203–212, 2003.
20. K. Mahrous, J. Bennett, G. Scheuermann, B. Hamann, and K. Joy. Topological segmentation in three-dimensional vector fields. *IEEE Transactions on Visualization and Computer Graphics*, 10(2):198–205, 2004.
21. A. Pobitzer, R. Peikert, R. Fuchs, B. Schindler, A. Kuhn, H. Theisel, K. Matkovic, and H. Hauser. The state of the art in topology-based visualization of unsteady flow. *Computer Graphics Forum*, 30(6):1789–1811, 2011.
22. Armin Pobitzer, Ronald Peikert, Raphael Fuchs, Holger Theisel, and Helwig Hauser. Filtering of ftle for visualizing spatial separation in unsteady 3d flow. In *Topological Methods in Data Analysis and Visualization II*, pages 237–253. Springer, 2012.
23. F. Sadlo and R. Peikert. Visualizing lagrangian coherent structures and comparison to vector field topology. In *Proceedings of the 2007 Workshop on Topology-Based Method in Visualization (TopoInVis)*, 2007.
24. Filip Sadlo. Lyapunov time for 2d lagrangian visualization. In *Topological and Statistical Methods for Complex Data*, pages 167–181. Springer, 2015.
25. Filip Sadlo and Ronald Peikert. Efficient visualization of lagrangian coherent structures by filtered amr ridge extraction. *IEEE Transactions on Visualization and Computer Graphics (Proceedings Visualization)*, 13(6), 2007.
26. Filip Sadlo, Alessandro Rigazzi, and Ronald Peikert. Time-Dependent Visualization of Lagrangian Coherent Structures by Grid Advection. In *Proceedings of TopoInVis (to appear)*. Springer, 2009.

27. Filip Sadlo and Daniel Weiskopf. Time-Dependent 2D Vector Field Topology: An Approach Inspired by Lagrangian Coherent Structures. *Computer Graphics Forum (to appear)*, 2009.
28. G. Scheuermann, H. Krüger, M. Menzel, and A. Rockwood. Visualizing non-linear vector field topology. *IEEE Transactions on Visualization and Computer Graphics*, 4(2):109–116, 1998.
29. Shawn C. Shadden, Francois Lekien, and Jerrold E. Marsden. Definition and properties of lagrangian coherent structures from finite-time lyapunov exponents in two-dimensional aperiodic flows. *Physica D*, 212(7), 2005.
30. Shawn C. Shadden, Francois Lekien, Jeffrey D. Paduan, Francisco P. Chavez, and Jerrold E. Marsden. The correlation between surface drifters and coherent structures based on high-frequency radar data in monterey bay. *Deep Sea Research Part II: Topical Studies in Oceanography*, 56(3-5), 2009.
31. H. Theisel. Designing 2D vector fields of arbitrary topology. *Computer Graphics Forum (Eurographics 2002)*, 21(3):595–604, 2002.
32. H. Theisel, Ch. Rössl, and H.-P. Seidel. Compression of 2D vector fields under guaranteed topology preservation. *Computer Graphics Forum (Eurographics 2003)*, 22(3):333–342, 2003.
33. H. Theisel, T. Weinkauf, H.-C. Hege, and H.-P. Seidel. Saddle connectors - an approach to visualizing the topological skeleton of complex 3D vector fields. In *Proc. IEEE Visualization 2003*, pages 225–232, 2003.
34. X. Tricoche, G. Scheuermann, and H. Hagen. A topology simplification method for 2D vector fields. In *Proc. IEEE Visualization 2000*, pages 359–366, 2000.
35. X. Tricoche, G. Scheuermann, and H. Hagen. Continuous topology simplification of planar vector fields. In *Proc. Visualization 01*, pages 159 – 166, 2001.
36. Markus Uffinger, Filip Sadlo, and Thomas Ertl. A time-dependent vector field topology based on streak surfaces. *Visualization and Computer Graphics, IEEE Transactions on*, 19(3):379–392, 2013.
37. T. Weinkauf, H. Theisel, H.-C. Hege, and H.-P. Seidel. Boundary switch connectors for topological visualization of complex 3D vector fields. In *Data Visualization 2004. Proc. VisSym 04*, pages 183–192, 2004.
38. T. Weinkauf, H. Theisel, H.-C. Hege, and H.-P. Seidel. Topological construction and visualization of higher order 3D vector fields. *Computer Graphics Forum (Eurographics 2004)*, 23(3):469–478, 2004.
39. Tino Weinkauf. *Extraction of Topological Structures in 2D and 3D vector fields*. PhD thesis, Otto-von-Guericke-Universität Magdeburg, Universitätsbibliothek, 2008.
40. M. Weldon, T. Peacock, G. B. Jacobs, M. Helu, and G. Haller. Experimental and numerical investigation of the kinematic theory of unsteady separation. *Journal of Fluid Mechanics*, 611, 2008.
41. R. Westermann, C. Johnson, and T. Ertl. Topology-preserving smoothing of vector fields. *IEEE Transactions on Visualization and Computer Graphics*, 7(3):222–229, 2001.
42. Alexander Wiebel, C. Garth, and Gerik Scheuermann. Computation of localized flow for steady and unsteady vector fields and its applications. *IEEE Transactions on Visualization and Computer Graphics*, 13(4):641–651, 2007.
43. T. Wischgoll and G. Scheuermann. Detection and visualization of closed streamlines in planar flows. *IEEE Transactions on Visualization and Computer Graphics*, 7(2):165–172, 2001.